The Astrophysical Journal, 797:108 (16pp), 2014 December 20 doi:10.1088/0004-637X/797/2/108

KILOPARSEC-SCALE PROPERTIES OF EMISSION-LINE GALAXIES

Shoubaneh Hemmati[1], Sarah H. Miller[1,2,3], Bahram Mobasher[1], Hooshang Nayyeri[1], Henry C. Ferguson[4,5], Yicheng Guo[6], Anton M. Koekemoer[4], David C. Koo[6], and Casey Papovich[7]
[1] University of California, Riverside, CA 92512, USA; shoubaneh.hemmati@ucr.edu
[2] University of California, Irvine, CA 92697, USA
[3] California Institute of Technology, Pasadena, CA 91125, USA
[4] Space Telescope Science Institute, Baltimore, MD 21218, USA
[5] Johns Hopkins University, Baltimore, MD 21218, USA
[6] UCO/Lick Observatory and Department of Astronomy and Astrophysics, University of California, Santa Cruz, CA 95064, USA
[7] Texas A&M University, College Station, TX 77843, USA
Received 2014 May 22; accepted 2014 October 13; published 2014 December 5

ABSTRACT

We perform a detailed study of the resolved properties of emission-line galaxies at kiloparsec scales to investigate how small-scale and global properties of galaxies are related. We use a sample of 119 galaxies in the GOODS fields. The galaxies are selected to cover a wide range in morphologies over the redshift range $0.2 < z < 1.3$. High resolution spectroscopic data from Keck/DEIMOS observations are used to fix the redshift of all the galaxies in our sample. Using the *HST*/ACS and *HST*/WFC3 imaging data taken as a part of the CANDELS project, for each galaxy, we perform spectral energy distribution fitting per resolution element, producing resolved rest-frame $U - V$ color, stellar mass, star formation rate (SFR), age, and extinction maps. We develop a technique to identify "regions" of statistical significance within individual galaxies, using their rest-frame color maps to select red and blue regions, a broader definition for what are called "clumps" in other works. As expected, for any given galaxy, the red regions are found to have higher stellar mass surface densities and older ages compared to the blue regions. Furthermore, we quantify the spatial distribution of red and blue regions with respect to both redshift and stellar mass, finding that the stronger concentration of red regions toward the centers of galaxies is not a significant function of either redshift or stellar mass. We find that the "main sequence" of star-forming galaxies exists among both red and blue regions inside galaxies, with the median of blue regions forming a tighter relation with a slope of 1.1 ± 0.1 and a scatter of $\sim$0.2 dex compared to red regions with a slope of 1.3 ± 0.1 and a scatter of $\sim$0.6 dex. The blue regions show higher specific SFRs (sSFRs) than their red counterparts with the sSFR decreasing since $z \sim 1$, driven primarily by the stellar mass surface densities rather than the SFRs at a given resolution element.

Key words: galaxies: evolution – galaxies: fundamental parameters – galaxies: kinematics and dynamics – galaxies: spiral

Online-only material: color figures

1. INTRODUCTION

Recent photometric and spectroscopic studies of galaxies show various trends in the evolution of their structural properties with redshift, leading to the populations of galaxies we see today. In particular, at intermediate redshifts, there is evidence for the growth of central bulges (e.g., Elmegreen et al. 2008; Daddi et al. 2007; Hopkins et al. 2010; Lang et al. 2014), formation and development of the Hubble sequence (e.g., Wuyts et al. 2011; Bell et al. 2012), disk growth (Miller et al. 2011), potential "disk settling" (Kassin et al. 2012), and quenching of star formation (e.g., Bell et al. 2004; Faber et al. 2007), all affecting observed global properties of galaxies.

However, despite extensive observational studies and theoretical simulations over the last decade, the specific details behind many of these processes are not well understood. For example, we do not yet know the underlying reason for the correlation between star formation rate (SFR) and stellar masses of star-forming galaxies and why the bulk of the star formation activity occurred early in the most massive galaxies (e.g., Noeske et al. 2007; Elbaz et al. 2007; Daddi et al. 2007). This relates to outstanding questions of how mass is assembled in galaxies and the efficiency with which gas is being converted into stars within different galaxy environments and feedback processes from star formation and active galactic nuclei (AGNs; van de Voort et al. 2011). It has also been shown that while passive galaxies play a significant part in measuring the global stellar mass density at higher redshifts, they have a minimal effect on the star formation density measurements, especially at later times (e.g., Dickinson et al. 2003; Rudnick et al. 2003; Nayyeri et al. 2014). Also, despite significant progress, it is not yet clear which parameters govern the star formation activity in galaxies and their dependence on look-back time (e.g., Lilly et al. 1996; Madau et al. 1998; Bell et al. 2005; Mobasher et al. 2009). Processes potentially responsible for this are a drop in the galaxy major merger rate (e.g., Patton et al. 2002; Lin et al. 2004; Bell et al. 2006; Lotz et al. 2011), exhaustion of the cold molecular gas (e.g., Tacconi et al. 2013; Daddi et al. 2010), or the occurrence of disk instabilities that cause the migration of gas into galaxy centers, creating bulges that stabilize the disk against further clump formation (e.g., Elmegreen et al. 2008; Dekel et al. 2009; Genzel et al. 2011; Wuyts et al. 2012; Guo et al. 2012).

While a number of studies have been performed to address these questions, they are largely based on the integrated properties of galaxies, without considering the details of the individual components and processes internal to galaxies. A physical understanding of the relations between various global properties of galaxies would not be complete without knowledge of the

processes involved at kiloparsec or smaller scales. Furthermore, one could achieve fundamental insights about the formation and evolution of galaxies by studying the relations between the integrated and internal (i.e., resolved) properties of galaxies over time. This requires deep multi-waveband images with high spatial resolution for representative samples of galaxies with available measurements of their global properties (i.e., stellar mass, SFR). With the advent of high resolution imaging detectors on the *Hubble Space Telescope* (*HST*), one can resolve kiloparsec-scale structures in galaxies along with their photometrically derived properties.

Over the last decade, extensive multi-waveband photometric surveys of galaxies have become available. The Cosmic Assembly Near-infrared Deep Evolution Legacy Survey (CANDELS; PIs: S. Faber and H. Ferguson; see Grogin et al. 2011 and Koekemoer et al. 2011) have provided high-resolution and deep images of galaxies in different passbands spanning the optical and near-IR wavelengths. Using the imaging data in the GOODS-S field, Wuyts et al. (2012) studied resolved colors and stellar populations of a complete sample of star-forming galaxies at $0.5 < z < 2.5$. The galaxies were selected to be massive ($>10^{10}\ M_{\odot}$) with high specific SFRs (sSFRs). The spectral energy distributions (SEDs) were constructed per bins of pixels of constant signal-to-noise and analyzed to study variations in rest-frame colors, stellar surface mass density, age, and extinction as a function of global properties of galaxies. They identified off-center clumps in galaxies and studied their contribution to the integrated SFR and integrated stellar mass. However, to fully understand the nature of these structures, one needs resolved spectroscopy.

Förster Schreiber et al. 2009 studied the properties of these stellar "clumps" for a sample of six star-forming galaxies at $z \sim 2$ using near-infrared integral field spectroscopy from SINFONI at the Very Large Telescope. This allowed measurement of the dynamical mass of the clumps and their spectral line emission diagnostic of star formation activity. Furthermore, they identified the "clumps" based on their emission lines (i.e., Hα emitting clouds) and used this information to study the nature of these structures. While this provides a superior technique for studying the kiloparsec-scale structure of galaxies, it is technically challenging. One could acquire such data with adequate signal-to-noise ratio (S/N) for only a handful of galaxies, making it difficult to generate a statistically large sample.

In the present paper, we take a combined approach. Using the latest optical and infrared imaging data in the CANDELS fields, we perform resolution element-by-element (i.e., pixel-by-pixel) SED fits to a sample of star-forming disk galaxies at $0.2 < z < 1.3$ with deep, spatially resolved high-resolution spectroscopy from Keck/DEIMOS (i.e., rotation curves) along their major axis. The spatially resolved spectra will make it possible to understand metallicity gradients and dynamics across galaxies as well as the relative timescales of various processes predicted to drive the formation of disks. We develop techniques to generate kiloparsec-scale resolved, self-consistent photometric maps allowing for differences in the image point-spread function (PSF) and resolution. We investigate how SFR and stellar mass surface density correlate in kiloparsec-scale structure and whether there is a difference in evolution with time between different regions inside galaxies. Full spectroscopic data will be utilized in subsequent papers in this series.

The structure of this paper is as follows. Section 2 presents the sample selection. In Section 3, we develop a method for performing resolved SED fitting, producing high resolution photometric maps of different observables in galaxies. In Section 4, we compare the integrated and resolved properties of galaxies. We present a technique for identifying physical regions in galaxies in Section 5. Results are presented in Section 6, discussed in Section 7, and summarized in Section 8. Throughout this paper, all magnitudes are in the AB system (Oke & Gunn 1983) and we use a standard cosmology with $H_0 = 70\ \mathrm{km\ s^{-1}\ Mpc^{-1}}$, $\Omega_M = 0.3$ and $\Omega_\Lambda = 0.7$.

2. SAMPLE SELECTION

The sample for this study is selected in GOODS-S and GOODS-N fields (Giavalisco et al. 2004) with available ground-based spectroscopy from DEIMOS (DEep Imaging Multi-Object Spectrograph; Faber et al. 2003) on Keck II.

The galaxies in this sample are selected to be brighter than 22.5 mag in the Advanced Camera for Surveys (ACS) F850lp filter and lie within the spectroscopic redshift range $0.2 < z < 1.3$. They have resolved, disklike structures, including not only well-formed spirals but also disturbed and morphologically irregular or abnormal systems. Early-type spheroids and unresolved objects were excluded from the sample. Finally, a magnitude limit of $K_s \leqslant 22.2$ is imposed to ensure a high fraction of reliable stellar masses.

Keck DEIMOS spectra were obtained for 236 galaxies that were selected using the above criteria (Miller et al. 2011). A total integration time of 6–8 hr wasacquired with the 1200 $\mathrm{l\ mm^{-1}}$ grating and $1''$ slits and a central wavelength of 7500 Å, achieving a spectral resolution of ~1.7 Å. Of the 236 targets, 129 of the galaxies (about 55% of the original sample) that were observed spectroscopically revealed resolved emission lines for which accurate rotation curves are measured (the emission extends beyond the seeing-dispersion PSF in the spectrum). Figure 1 shows that the distribution of sizes or masses of our selected targets is not biased with redshift or magnitude compared to galaxies with the same redshift and magnitude cut.

This sample is most desirable for studying resolved properties of galaxies for the following reasons.

1. Seven high resolution *HST* optical and infrared images taken by ACS and Wide Field Camera 3 (WFC3) from the CANDELS are available. It has been shown that using optical+NIR filters reduces the uncertainties in studying resolved properties in galaxies compared to using optical filters only (Welikala et al. 2011). In this study, we use *HST*/ACS observations in the F435W, F606W, F775W, and F850LP (hereafter B_{F435W}, V_{F606W}, I_{F775W}, and Z_{F850lp}) and *HST*/WFC3 observations in the F105W, F125W, and F160W (hereafter Y_{F105W}, J_{F125W}, and H_{F160W}) filters. The ACS images have been multi-drizzled to the WFC3 pixel scale of $0\farcs06$ (Koekemoer et al. 2011).
2. Spectroscopic redshifts for all the galaxies are available. One of the major sources of uncertainty in measuring galaxy properties through fitting their spectral energy distribution is the uncertainty in their photometric redshift. We overcome this issue by knowing the precise spectroscopic redshift of the galaxy.
3. Kinematic information is available with high spectral and spatial resolution for rotation curves and dynamical models of all the galaxies in this sample. This allows direct comparison between high resolution photometric maps (of stellar mass, SFR, etc.) and dynamical information on kiloparsec scales.

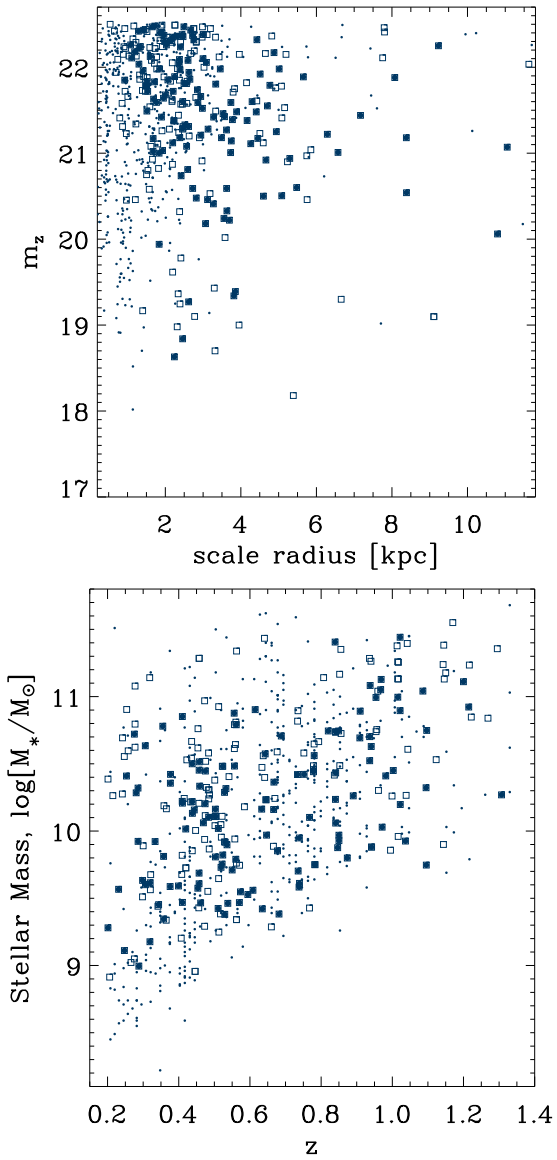

Figure 1. Apparent magnitude (z_{F850lp}) vs. disk scale radii (in kiloparsecs) and stellar mass vs. redshift for galaxies selected for the present study, consisting of 129 resolved emissions (large filled squares). There are 107 galaxies that also satisfy the selection criteria here, with available spectroscopic data but unresolved or undetected emission (empty squares). These are not included in the analysis in this study. A control sample is also shown with similar photometric redshift and magnitude cuts (small dots).

(A color version of this figure is available in the online journal.)

3. RESOLVED MAPS OF GALAXIES

In this section we explain the step-by-step method we develop to make resolved rest-frame optical color, stellar mass, SFR, age, and extinction maps by performing spectral synthesis fitting per resolution element for each galaxy.

3.1. Cutouts

The very first step in making resolved maps of galaxies is to make sure that we are combining the same resolution and pixel scale in different images. The pixel scales of CANDELS *HST* images are all set to 0.″06. However, we need to PSF-match these images across the range of the filters used. We take all lower resolution images to the resolution of F160W which has the longest wavelength coverage.

We make 14 cutouts (seven band *HST* images + their corresponding weight maps) each of 200 × 200 pixels. We construct the PSF for each band using the IDL routine PSFGEN.PRO and perform PSF matching using the IRAF PSFMATCH task. This gives a spatial resolution of ∼0.″17. After matching the resolutions, we make smaller cutouts of 80 × 80 pixels which, at the redshift range of our sample, correspond to a box size of ≈15–40 kpc (see Figure 2).

We removed 10 galaxies located at the edge of the fields because the constructed PSF is not a good representation of the true PSF at these locations due to distortion, lower exposures, and signal-to-noise level. The final results are sensitive to this as a wrong PSF kernel would lead to ripples in the final maps. Fitting Gaussians to the PSFs before performing the PSF matching would clear this issue; however, for the sake of consistency, we discard these 10 galaxies. This leaves us with 119 galaxies.

To define the boundary of the galaxy, we run the SExtractor code (Bertin & Arnouts 1996) on the z-band cutouts (seen in Figure 2). Of all the ACS bands, the z band reveals the deepest, smoothest, most extended light. This feature is seen in most of the galaxies in our sample. The segmentation maps of each galaxy, produced by SExtractor, are then multiplied by the cutouts to mask the low surface brightness outskirts of galaxies.

3.2. SED Fitting per Resolution Element

One of the most widely used methods for studying the physical properties of galaxies (e.g., stellar masses, star formation histories and rates, metallicities, ages) at different redshifts is to fit their observed SEDs with stellar population synthesis models. While many sources of uncertainties in the models and fitting methods still exist, there has been huge progress in finding statistical properties of galaxies at all redshifts (e.g., Reddy et al. 2012; Conroy 2013).

Here we apply this technique to the SEDs per resolution element in each galaxy instead of its integrated light (e.g., Zibetti et al. 2009; Welikala et al. 2011; Wuyts et al. 2012; Lanyon-Foster et al. 2007). At the most basic level, resolved SED fitting allows the analysis of substructures in any given galaxy and reduces the uncertainties caused by using an "average" dust attenuation law and star formation history for the whole galaxy. For each galaxy, we build a multi-wavelength catalog. Each row in the catalog corresponds to a resolution element inside the galaxy with the four-band ACS, three-band WFC3, their corresponding RMS errors, and the spectroscopic redshift of the galaxy.

The first phase of the SED-fitting process is to generate an inclusive library of model SEDs that span a wide range in parameter space. We use the PICKLES library for stars (Pickles 1998), different synthetic and composite quasar libraries available in the LePhare package (Arnouts et al. 1999; Ilbert et al. 2006), and BC03 models (Bruzual & Charlot 2003) for the galaxy library. While the relative contribution of thermally pulsating asymptotic giant branch stars is still uncertain, it has been shown in previous studies that the Maraston (Maraston et al. 2006) models overpredict the near-infrared luminosity (Kriek et al. 2010) compared to BC03. We assume a Chabrier (Chabrier 2003) stellar initial mass function (IMF). Extinction values range from zero to one using the Calzetti Starburst and 57 different ages ranging from zero to the age of the universe at the spectroscopic redshift of the galaxy. We adopted single burst, constant, and exponentially declining star formation histories. We fix the metallicity to 40% solar to mitigate the fitting degeneracies by

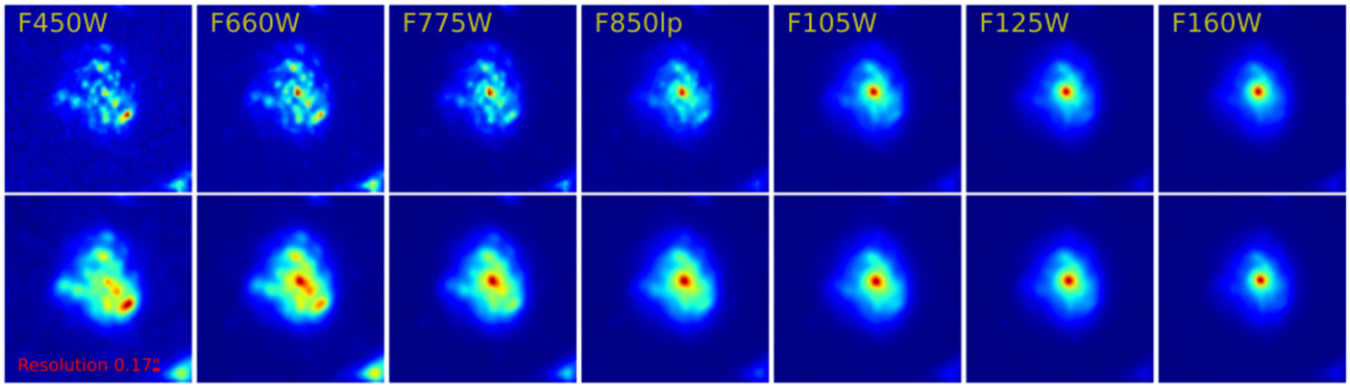

Figure 2. Seven-band *HST* 80 × 80 pixel cutouts of a typical galaxy from our sample at $z = 1.1$ (80 pixel = 39.7 kpc) before and after PSF matching in top and bottom rows, respectively.

(A color version of this figure is available in the online journal.)

Table 1
Parameters for BC03 Models

Parameters	Number	Range
Age (Gyr)	57	0.01–13.5 [a]
Extinction $E(B-V)$	15	0.0–1.0 [a]
τ (Gyr)	21	0.001–10.0 [a]
Metallicity		40% $Z_\odot$

Note. [a]Not equally spaced.

shrinking the library size (see Table 1). We explore the effects of choosing this particular grid in the Appendix by comparing it to models with different metallicities, star formation histories, and different resolutions in extinction and age.

After finalizing the library, we fit the observed flux per resolution element to our model SEDs. For this we use the LePhare code, an SED-fitting code based on χ^2 minimization. After fixing the redshifts to their spectroscopic values, we fit the SEDs to find the closest match from the model library created for that specific redshift and measure the physical information associated with the galaxy (absolute magnitudes, stellar mass, SFR, age, and extinction). The physical parameters from the SED fitting output in this work correspond to the median of the probability distribution function marginalized over all other parameters. We use 16% lower and 16% higher values from the maximum likelihood analysis to measure the 1σ error for each parameter.

We use the best-fit template to estimate the $(U-V)_{\text{rest-frame}}$ colors per resolution element. The U-band response function here corresponds to the Johnson filter. We choose this rest-frame optical color to span the Balmer/4000 Å break. It has been shown that the Balmer/4000 Å break feature is not only very sensitive to stellar ages (e.g., Kauffmann et al. 2003; Nayyeri et al. 2014), but that the strength of this break strongly correlates with the width of Hα and the best-fit sSFR (Kriek et al. 2011). Therefore, using passbands straddling the Balmer break is optimized for our purpose, and provides great insight on the star formation histories of substructures in galaxies.

The high resolution maps measured through the SED fits per resolution element, are presented in Figures 3 and 4 for a subsample of galaxies.[8] These show the $(U-V)_{\text{rest-frame}}$ color, weight, stellar mass surface density, star formation surface density, extinction, and age and their 1σ error maps for example galaxies from the sample. Unlike the more normal Hubble-type galaxy morphologies in Figure 3, Figure 4 shows two examples of galaxies with abnormal features such as blue nuclei (AGNs) or disturbed, interacting morphologies.

In $(U-V)_{\text{rest-frame}}$ maps, there is a general tendency toward a central red bulge and some blue regions in the overall green disk (Figure 3). There are three clear exceptions in our sample with the nuclear region in the galaxy significantly bluer than its surroundings (e.g., see the first column in Figure 4). These are examples of "blue-nucleated galaxies" (Schade et al. 1995; Abraham et al. 1999). These three galaxies have Chandra X-ray detections (matched with a 1″ radius), which suggest the presence of an AGN at their centers. Interestingly, even though we include quasar libraries while performing the SED fitting, none of the central elements in these galaxies were "best" fitted to these templates. In future works, we will investigate whether adding dust to the quasar models alters the fitting/color of the central resolution elements in these galaxies. The $(U-V)$ *weight* maps, which will be used to identify different regions inside galaxies in the following sections, are calculated from the square root of the sum of squares of fluxes in the U and V bands and normalized to the maximum value.

Contrary to the UV–optical color maps which often show "clumpy" structures, the stellar mass surface density maps are mostly smooth with most of the mass concentrated in the bulge. The same trend was also reported in Wuyts et al. (2012) for galaxies at somewhat higher redshifts from $1 < z < 2$. Lanyon-Foster et al. (2012), however, claims that the smoothness of the stellar mass maps neither holds true for all galaxies nor for all features seen.

To further examine the absence of structure in the stellar mass maps, we smooth them with a Gaussian of width σ (where σ is the dispersion of stellar mass surface density over all resolution elements) and subtract them from their respective unsmoothed stellar mass maps. Weighting the residual by the stellar mass error, the structure residuals in all galaxies account for less than 1.2% of their total stellar mass surface density. Wuyts et al. (2012) find a similar 2%–3% of the total stellar surface density in the clumps as defined by either rest-frame U- or V-band maps of Voronoi-binned pixels for galaxies from $0.5 < z < 1.5$.

The SFR surface densities are directly derived from the SED fitting. Estimating the SFRs from the SED is very challenging due to both the age–dust–metallicity degeneracy and the choice of SFH prior, especially at high redshifts (Conroy 2013).

[8] Maps of all galaxies in the sample are at: http://www.shouby.com/research/disk-galaxies/.

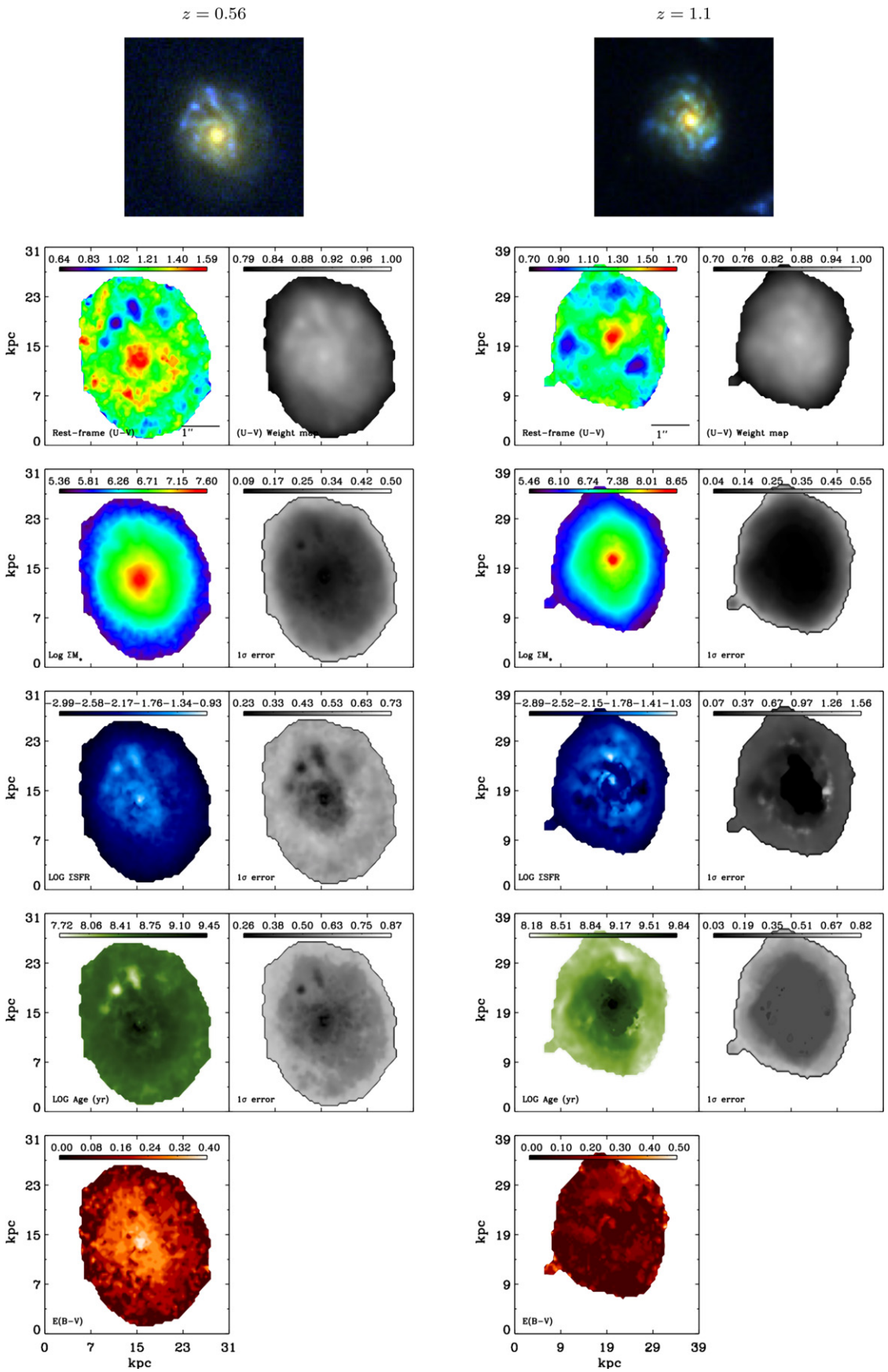

Figure 3. Top to bottom: stacked BZH color image, rest-frame ($U - V$) color, rest-frame color weight, stellar mass surface density and 1σ error, star formation surface density and 1σ error, stellar age and 1σ error, and extinction maps (LePhare does not produce uncertainties for extinction) for two galaxies at $z = 0.56$ (left) and 1.1 (right).

(A color version of this figure is available in the online journal.)

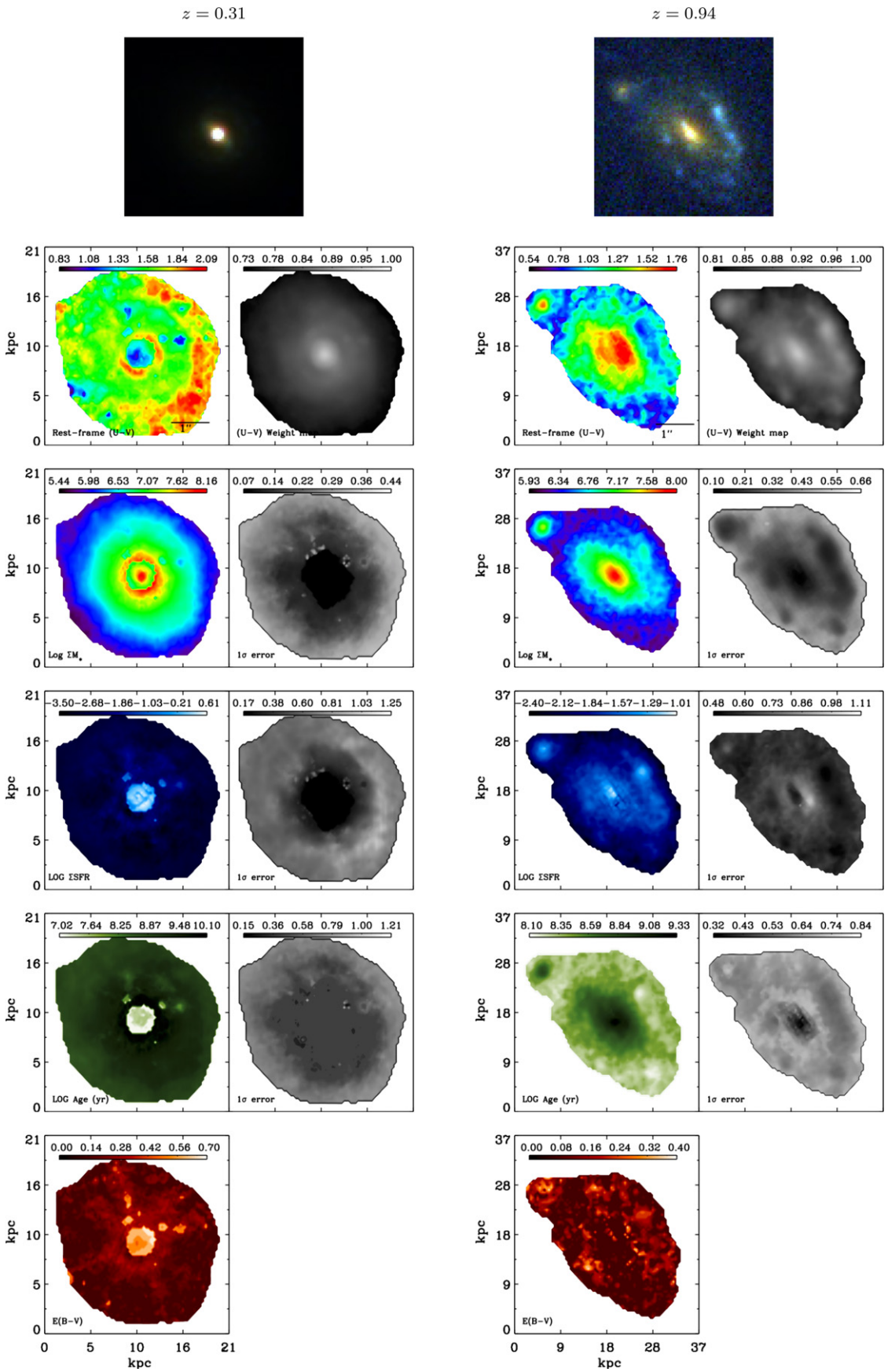

Figure 4. Same as Figure 3, but for two of the galaxies with abnormal or disturbed features or signs of interaction. Respectively from left to right, a galaxy at $z = 0.31$ with a blue $(U - V)$ nucleus hosts an AGN at its center (NB artificial ripples in the maps induced by the bright AGN source). The right panel shows a galaxy at $z = 0.94$ with signs of interaction or minor merging.

(A color version of this figure is available in the online journal.)

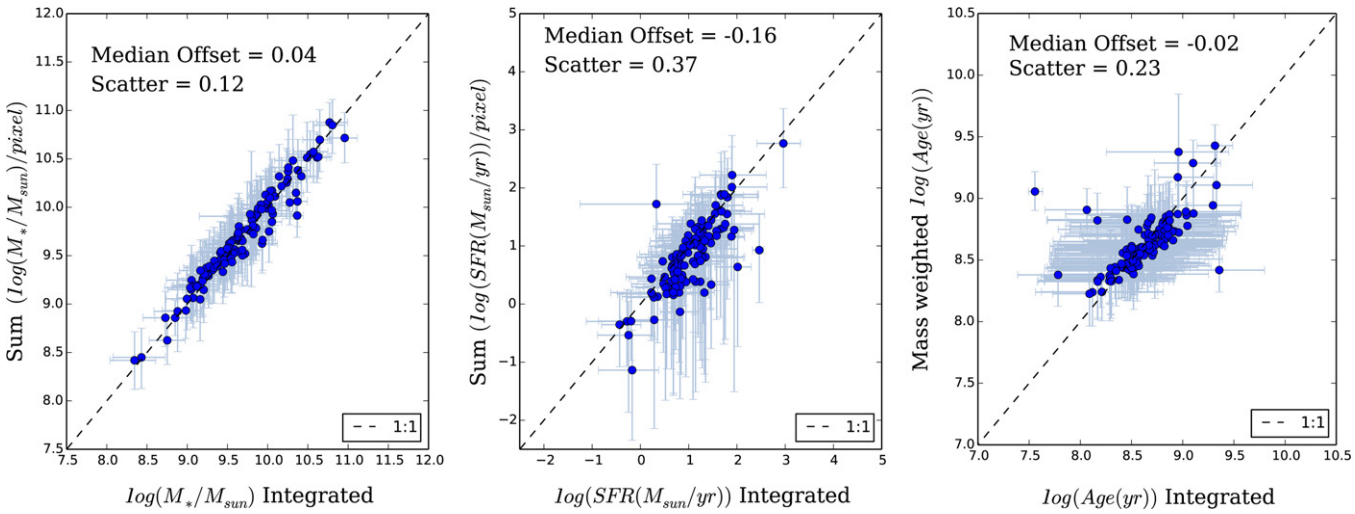

Figure 5. Comparison between resolved and integrated properties: (left) integral of stellar mass surface density per resolution element vs. integrated stellar mass, (middle) integral of SFR surface density per resolution element vs. integrated SFR, and (right) mass-weighted stellar age vs. integrated age of the galaxies.
(A color version of this figure is available in the online journal.)

However, it has been shown that at $z < 1$ this is less of an issue and SFRs derived by fitting the SED agree very well with the other indicators of SFR with less than 0.23 dex scatter (Salim et al. 2009).

4. INTEGRATED VERSUS RESOLVED PROPERTIES

In this section, we examine the consistency between resolved measurements and those derived for the entire galaxy. We measure the photometry of galaxies in the same seven *HST* bands by adding up the fluxes within the boundary defined by the segmentation map of the galaxy. We estimate the "global" stellar mass, SFR, and mean stellar age for each galaxy by fitting the integrated fluxes with the same model library used in the previous sections.

In the first panel of Figure 5, we compare the integrated stellar masses with the sum of stellar masses measured per resolution element. We find a median offset of 0.04 dex and a scatter of 0.12 dex for stellar masses. Wuyts et al. (2012) reported no median offset using Voronoi-binned pixels rather than individual pixels. This is contrary to some of the previous works which found larger disagreement, with the global mass being lower than the integral of masses over resolution elements up to 40% for a sample of nearby galaxies (Zibetti et al. 2009). The small offset can be explained by lower estimates of M/L from the integrated fluxes due to more luminous young stars in the disk (e.g., Papovich et al. 2001; Shapley et al. 2001).

Comparing the resolved and the integrated SFRs, we find a median offset of 0.16 dex with a scatter of 0.37 dex (Figure 5, middle plot). In a similar study (Wuyts et al. 2012), a larger offset of 0.27 dex in the opposite direction was found. The SFR estimates from the SED-fitting have different sources of uncertainty. This makes explaining the offset very challenging. One possible source of the offset is due to the overcorrection for dust extinction and hence slightly larger SFRs (in 90% of the galaxies in the sample the average $E(B-V)$ over resolution elements is less or equal to the $E(B-V)$ estimate for the galaxy).

For the stellar age comparison, we calculate the stellar mass weighted age from the resolved SED fits. The right panel in Figure 5 shows the comparison of resolved and integrated stellar ages. A very small offset of 0.02 dex with a scatter of 0.23 dex is observed. This median offset is 10 times smaller than that of Wuyts et al. (2012). The plausible explanation for this small offset is that using the stellar mass-weighted age rather than light-weighted age would make outshining of older more massive stars by younger less massive stars (e.g., Papovich et al. 2001; Maraston et al. 2010) less of an issue.

5. IDENTIFICATION OF RED AND BLUE REGIONS IN GALAXIES

To allow the study of substructures in galaxies at kiloparsec scales, we identify regions based on the resolved photometric maps. This is based on the $(U-V)_{\rm rest-frame}$ color maps. Most of these regions are kiloparsec size with comparable characteristics to what are called "clumps" in many previous studies (e.g., Guo et al. 2012). However, we remain agnostic regarding the nature of these regions, preferring this descriptor over the term "clump," given that the latter connotates a distinct entity within the galaxy, potentially even a distinct self-gravitational mass, which may not be accurate. This becomes clear when comparing the physical differences between the regions identified, based on rest-frame optical color, rest-frame UV image, and stellar mass maps (S. Hemmati et al., in preparation). Using the available deep spectra and kinematic information, in future work we aim to more precisely evaluate which regions are gravitationally bound "clumps" and which regions are simply differentiated by their relative star formation or dust properties with respect to the surrounding parts of the galaxy.

In this section, we first describe our method of identifying regions in our galaxies, red and blue in this case, and proceed by looking at their properties.

5.1. Region Identification

We select red and blue regions inside galaxies by fitting weighted rest-frame color distributions in each galaxy to Gaussian functions. We used the $(U-V)$ weight maps described in the previous section to avoid selecting insignificant regions at the very edges of galaxies with very low surface brightness. We plot the distribution of weighted rest-frame color for each galaxy. We choose the bin size following Scott's rule, which is optimal for normally distributed data (Scott 1979). We then

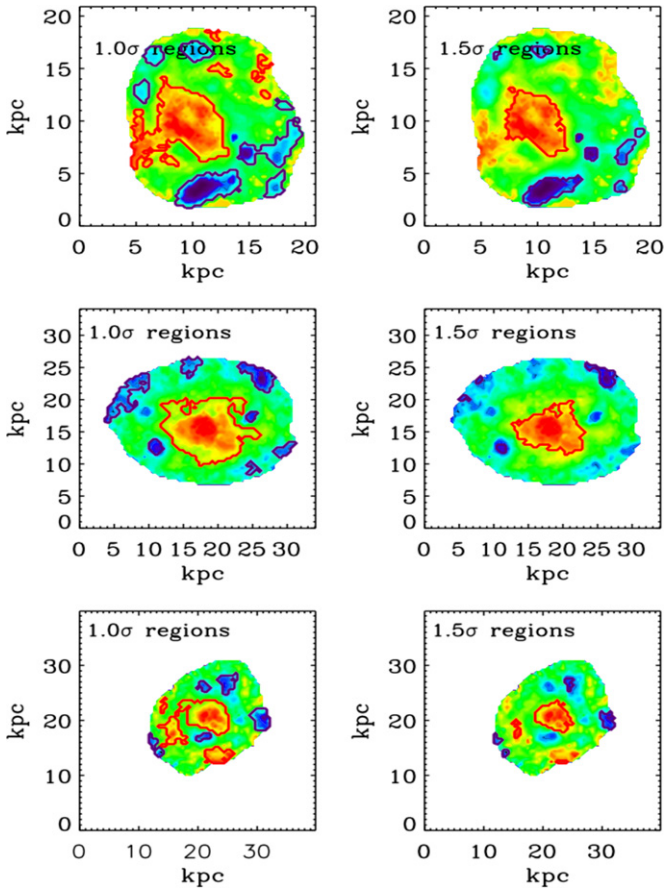

Figure 6. Red and blue regions identified by contours on $(U - V)$ rest-frame color maps for three example galaxies at $z = 0.29$, 0.69, & 1.21, respectively, from top to bottom. Left panels correspond to regions above and below the *middle peak* $\pm$ 1σ and right panels correspond to regions above and below *middle peak* $\pm$ 1.5σ.

(A color version of this figure is available in the online journal.)

fit the color distribution with three skewed Gaussians, one for fitting the median color of the galaxy and the other two allowing for the bluer or redder regions with centers constrained at two sides of the central peak. This is done to build high-pass (red) and low-pass (blue) filters based on the relative color distribution for each galaxy. Specifically, we do this by taking the *middle peak* + 1.5σ for the red regions and *middle peak* $- 1.5\sigma$ for the blue regions (here after 1.5σ regions).

We examine different filtering sigma thresholds identifying the regions. Setting higher sigma values would only select regions with the most contrast while choosing a smaller sigma factor would be sensitive to lower levels of "unsmoothness" closer to the noise level. Another advantage of this method is that the middle Gaussian identifies the "green" or intermediate color properties of the distribution. For our purposes in this paper, we find that 1.5σ regions most closely match our visual intuition for red and blue regions of color (see Figure 6).

We then run SExtractor on the high and low pass filtered color images with the SExtractor configuration file carefully optimized by visual inspection of all selected regions. The same configuration file for blue and red regions was used. We did not use any filter (e.g., Gaussian, top-hat) to avoid introducing any resolution elements from outside of the region area identified by the filters. SExtractor will provide us with two segmentation maps per galaxy for the red and blue filtered images, which we use to build the region map for each galaxy.

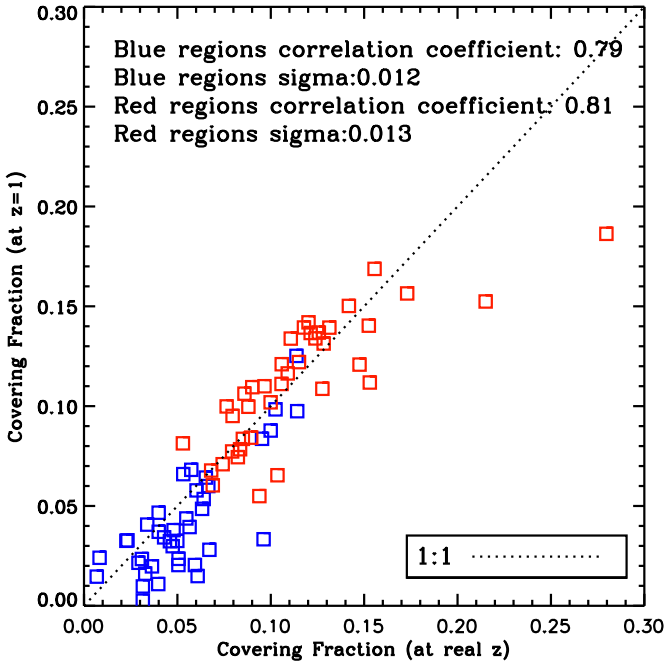

Figure 7. Covering fraction of red and blue regions inside galaxies redshifted to $z = 1$ vs. the covering fraction at their real, observed redshift. Blue/red squares represent the covering fraction of blue/red regions, respectively.

(A color version of this figure is available in the online journal.)

Here we take advantage of the dual mode features of SExtractor to estimate properties of the regions. In dual mode, the sources are detected in the first image and the photometry is then performed on the second image based on those detections. We use the color maps as our detection image and use the mass maps as our second image. This way, we not only know the area and position of each identified region based on the segmentation maps, we also know their corresponding stellar masses. We measure this by converting our stellar mass surface density maps from a logarithmic to a linear scale, measuring the isophotal flux output from SExtractor for each galaxy (this is the best choice for our purpose with no assumption depending on the shape). In this work we do not a priori decompose the bulge from the disk, to minimize assumptions on region definitions, however, there are GALFIT bulge-to-disk decompositions for all galaxies in the sample from Miller et al. (2011), and we confirm that bulges are consistently identified as red regions between the two methods with the exception of the three galaxies with blue nuclei mentioned above.

5.2. Redshift-dependent Bias

Since the pixel size is fixed for all the images, the apparent change due to redshift in the intrinsic angular size of galaxies is likely to introduce a bias in the way the regions are identified and in their estimated size. Here we examine the presence of such biases by simulating the images of galaxies. We artificially redshift galaxies from $0.3 < z < 0.5$ to $z = 1.0$ and re-identify their regions using the same technique.

By identifying regions based on color maps rather than a parameter sensitive to surface brightness dimming, any redshift-dependent bias could be better revealed. The dimming factor is redshift dependent (not wavelength dependent) and thus, the primary redshifting effect we need to account for is the relative change in observed angular size, a, with redshift. Assuming a_0 and a_i to be the angular sizes of the same galaxy at redshifts z_0

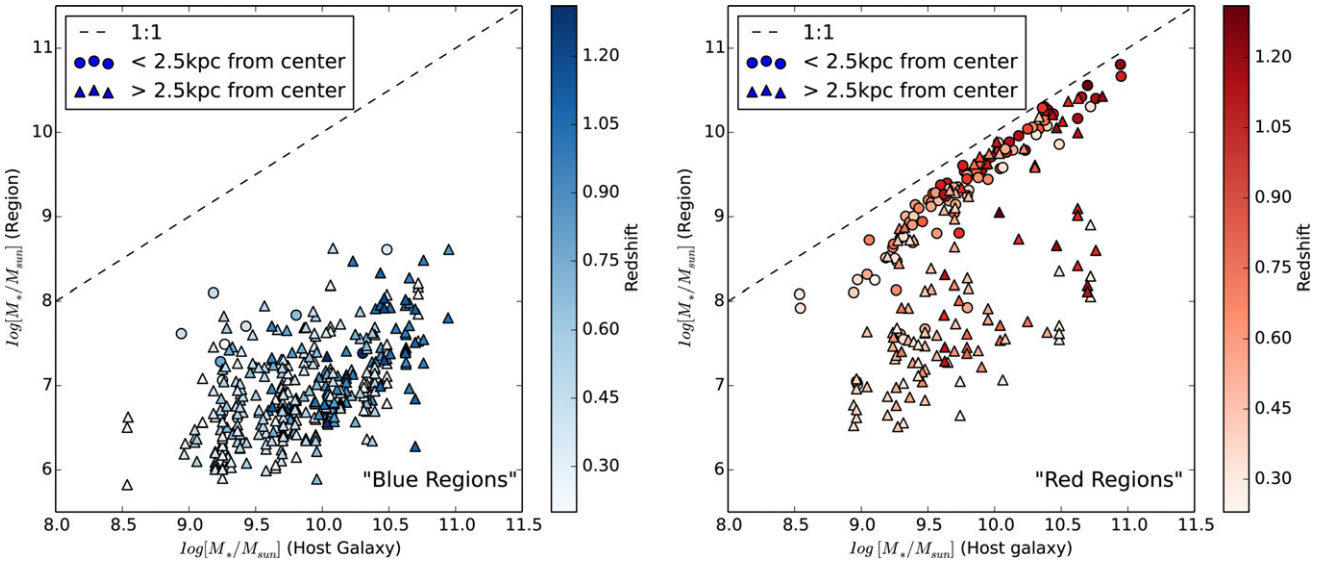

Figure 8. Stellar mass of red and blue regions vs. stellar mass of the host galaxy in the right and left panels, respectively. Filled circles (triangles) represent regions with distances less (more) than 2.5. In both panels, the lighter color corresponds to lower redshift.

(A color version of this figure is available in the online journal.)

and z_i, respectively, and d_0 and d_i being the luminosity distances corresponding to these redshifts (Barden et al. 2008), we have $a_o/a_i = (d_i/(1+z_i)^2)/(d_o/(1+z_o)^2)$.

We shift galaxies within the observed redshift range $0.3 < z < 0.5$ to $z_{\rm rest-frame} = 1$, and for each galaxy identify the blue and red regions at the two redshifts (the observed redshift and at $z = 1$). We then estimate the covering fractions of these regions and compare them in Figure 7. We define covering fractions by normalizing the area within blue and red regions to the total area of a galaxy, defined based on the number of resolution elements in the segmentation maps of both the regions and galaxies. The linearity of the relation and small scatter ($\sigma \simeq 0.01$) around the 1:1 line in Figure 7 confirms that there is no significant bias due to cosmological angular size evolution for our region selection method at higher redshifts ($z \simeq 1$) as compared to lower redshifts in our sample.

6. RESULTS

6.1. Physical Properties of the Regions and Small-scale Properties of Galaxies

In Figure 8, we plot the stellar mass of each identified region as a function of total stellar mass, color-coded by redshift. There is an overall trend of more massive regions being in more massive hosts and an interesting bimodal behavior seen in the distribution of red regions. To explore the extent to which the tight sequence of high-fraction red regions are bulges or central spheroidal components, we divide the regions into two groups based on their distance from the center of the galaxy (Figure 8). Circles show regions closer than 2.5 kpc to the center and triangles represent regions farther than 2.5 kpc from the center (where region centers are calculated using SExtractor). More than 98% of blue regions are farther than 2.5 kpc from the center. Forty-five percent of the red regions are located within the 2.5 kpc of the center, 90% of which contribute around 30%–90% to the total stellar mass of the host galaxy. It is worth noting that 2.5 kpc is an arbitrary cut chosen for simplicity rather than binning in distance. The red regions that are farther than 2.5 kpc from the center (red triangles) are likely to be dustier regions in the disk. This will be explored further in future work by cross-correlating the mass and extinction maps. It is possible many central components could be dusty star-forming regions as well rather than relatively passive spheroidal components like classical bulges.

We now examine the evolution of the relative area covered by blue and red regions inside each galaxy, with respect to both the redshift and the total stellar mass of each galaxy. Figure 9 plots the covering fraction of blue and red regions as a function of redshift and stellar mass. Clearly, the covering fractions of red regions are always larger than blue regions. Also, the dispersion in the distribution of the covering fractions for red regions is consistently larger than that for the blue. Furthermore, we find no significant evolution with either redshift or stellar mass in the covering fraction of blue or red regions. This supports the paradigm that small-scale properties of galaxies on average are not evolving much over intermediate redshifts.

For the blue and red regions, we measure distances from each of their associated resolution elements to the center of their respective galaxies as defined by the rotation curve. We then normalize to the scale radius of the galaxy to avoid biases due to the evolution of galaxy size across redshift. Figure 10 shows the median and dispersion of distances from the center of the galaxy for both blue and red regions versus redshift and total stellar mass, respectively. Blue regions are almost always farther away from the center of the galaxy than red regions with a larger dispersion in the distribution of distances. Since the red regions are often found to be synonymous with the bulge, the increase of the weight and strength of this red bulge region (manifested by the decrease in scatter) with the stellar mass can be seen in Figure 10. There is no significant evolution in the median distance (scaled by the radii of the galaxy) of red or blue regions from the center with time in the redshift range covered in this study. However, there is a slight increase in the median distance between blue and red regions in more massive galaxies compared to the least massive galaxies.

In order to study the physical nature of the red and blue regions, we compare the distributions of median mass, SFR, age, and sSFR for the regions associated with each galaxy in our sample (Figure 11). To account for the effect of redshift (a resolution element at low redshift corresponds to a smaller

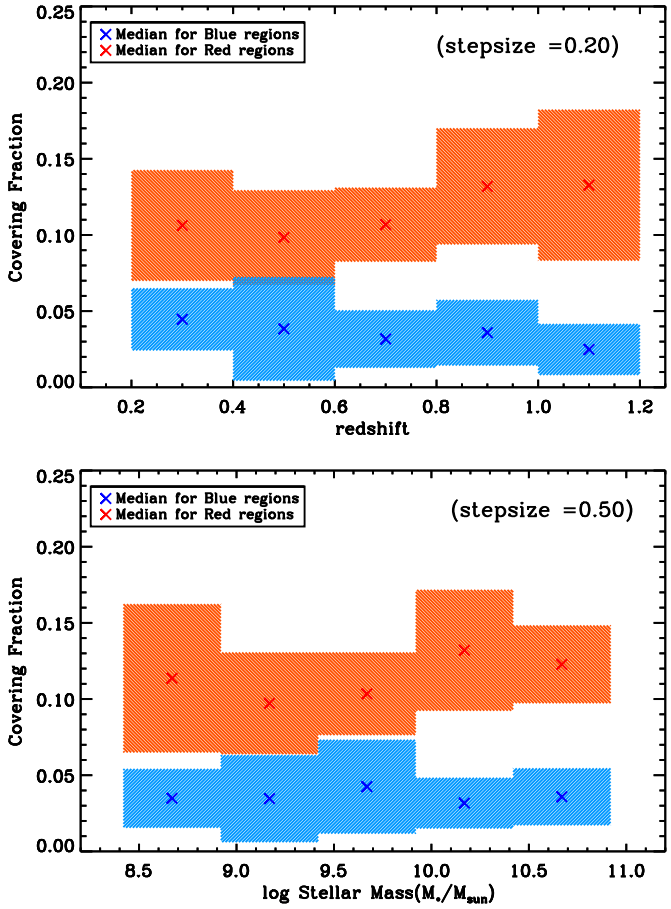

Figure 9. Covering fraction of red and blue regions inside galaxies (area of identified red or blue regions divided by the area of the galaxy) as a function of redshift and stellar mass in top and bottom panels, respectively. Crosses show the median in each bin and the shaded area shows the 1σ dispersion.

(A color version of this figure is available in the online journal.)

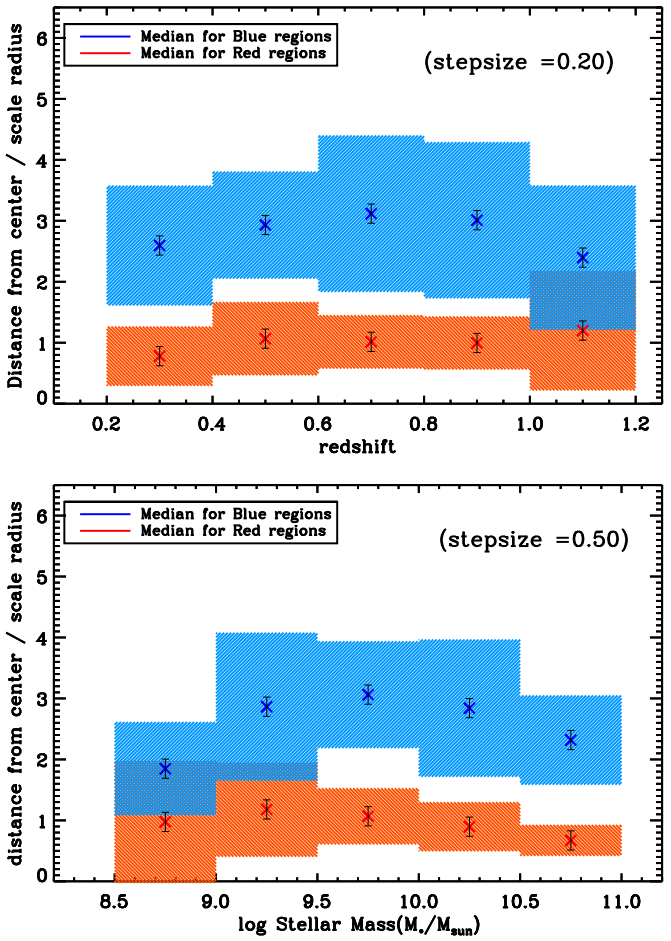

Figure 10. Spatial distribution of red and blue regions in their host galaxies. The figure shows the distance of blue and red regions from the dynamical center of the galaxy as a function of redshift and stellar mass of the host galaxy. Cross symbols represent the median in each bin, error bars are measurement errors, and the shaded region shows the dispersion of distances of resolution elements in the identified regions for galaxies at each bin. Blue regions are always at larger distances from the center of the galaxy compared to red regions.

(A color version of this figure is available in the online journal.)

area than at higher redshifts), we normalized each value by the physical area of a resolution element at the spectroscopic redshift of the galaxy. While red and blue regions are identified solely based on rest-frame ($U - V$) colors, there is a clear distinction between their stellar mass surface density, age, and sSFR distribution. However, they have similar SFR surface densities. As in most of our galaxies, especially as mass increases, the bulge, central pseudo-bulge, or central disk contributes to a significant portion of the red regions. It is in the red regions where the highest concentration of stellar mass exists. It is also clear that the distribution of stellar ages in blue regions peaks at younger ages even though the overall distribution of SFRs is similar to that in red regions.

6.2. Main Sequence of Star-forming Galaxies

There is a strong correlation between the SFR and stellar mass "*main sequence*" in star-forming galaxies out to high redshifts (e.g., Lilly et al. 2013; Salmon et al. 2014), with the bulk of star formation occurring in more massive galaxies rather than in less massive systems (e.g., Noeske et al. 2007; Bell et al. 2005; Reddy et al. 2006; Elbaz et al. 2007). A population of passive galaxies also exists, located below the main sequence, whereas starbursts lie above. Wuyts et al. (2013) showed evidence that star formation and assembled stellar mass are also correlated on a subgalactic scale. We present the SFR–stellar-mass relation for the blue and red regions in our galaxies in Figure 12. Each red/blue point on the plot demonstrates the median of SFR and mass over resolution elements associated with red/blue regions in any given galaxy.

There is a clear bimodality between the red and blue regions with red regions having a higher stellar mass compared to blue regions at a fixed SFR. The blue regions form a tight relation with a scatter of ∼0.2 dex which is three times less than that seen in the red regions (∼0.6 dex). This agrees with the spread in the SFR for red regions shown in Figure 11. The best linear fit to the blue and red regions, shown with solid lines, has a slope of 1.1 ± 0.1 and 1.3 ± 0.1, respectively. This is steeper compared to the relation seen for integrated main-sequence galaxies (Elbaz et al. 2007) extrapolated to lower stellar masses. However, this is consistent with a recent work by Whitaker et al. (2014), studying lower mass systems ($\log(M_*/M_{\rm sun}) < 10$) and finding a slope of ∼1.0 roughly constant over the redshift range $0.5 < z < 2.5$. We also show the relation between the sSFR and median stellar mass where blue regions have a higher sSFR compared to red regions, a trend that does not appear to depend on median stellar mass of the region in this projection, however, this changes as we account for the stellar mass of the sample as a function of redshift.

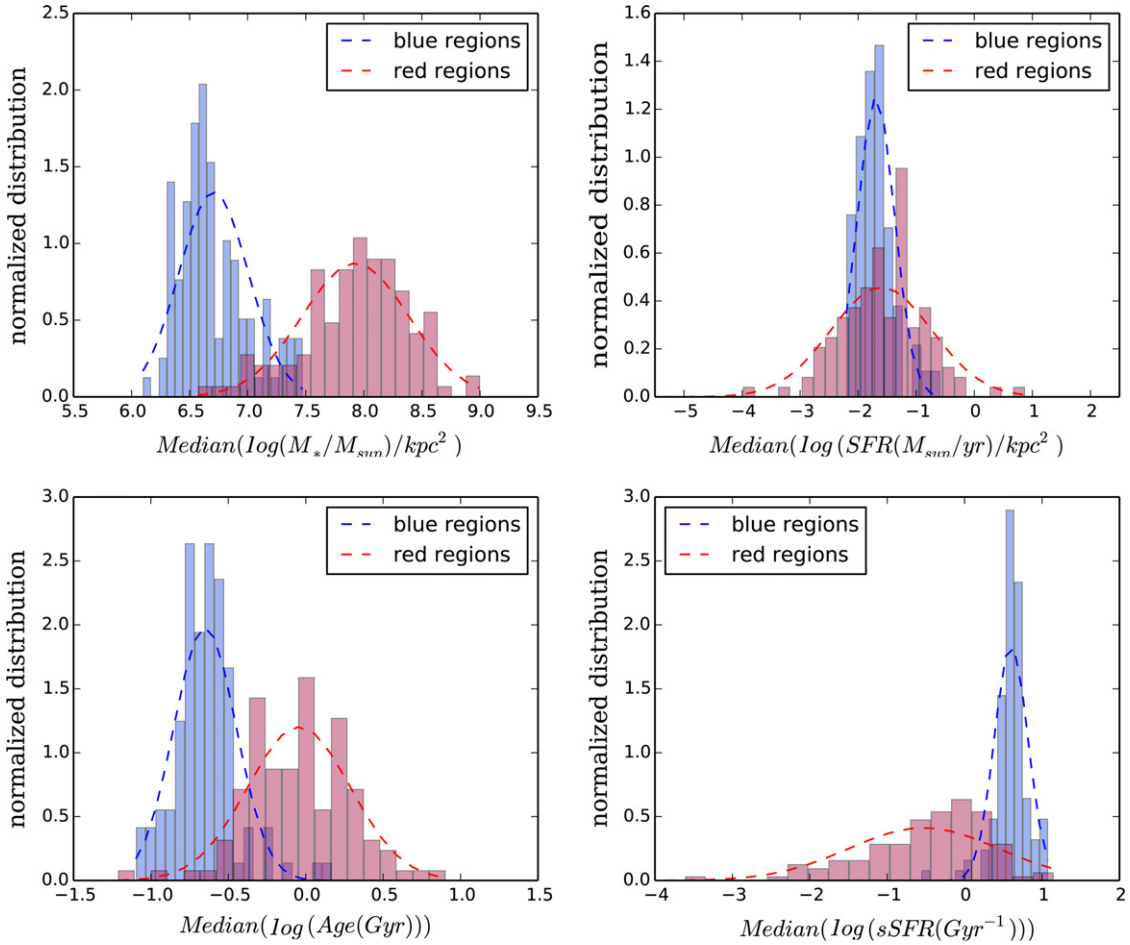

Figure 11. Physical properties of the blue and red regions in galaxies. Histogram of median values of stellar mass surface density, star formation rate surface density, stellar age, and sSFR are plotted from top left to bottom right, respectively. Dashed curves are Gaussian functions fitted to each histogram.

(A color version of this figure is available in the online journal.)

The sSFR is known to evolve over intermediate to low redshifts with both redshift and stellar mass of the galaxies (e.g., Feulner et al. 2005). In Figure 13, we present a three-dimensional plot of the sSFR versus redshift versus stellar mass surface density for individual resolution elements belonging to red (left) or blue (right) regions. The sSFR of red regions decreases as the stellar mass increases for all redshifts. The same overall trend can be seen among resolution elements in blue regions. Binning by stellar mass, we fit a function of the form sSFR $\propto (1+z)^b$ to the sSFR per resolution element in red and blue regions. This is plotted in Figure 14 where we see an increase in the b value with increasing stellar mass. It is known that at any given redshift, the mean sSFR is smaller for high mass galaxies (Damen et al. 2009). In the context of "downsizing," more massive galaxies formed their stars before less massive systems (Cowie et al. 1996). The trend that we see here for substructures in galaxies is very similar to bluer less massive regions having higher sSFRs compared to red regions. This implies that the more massive regions have assembled more of their mass at earlier times.

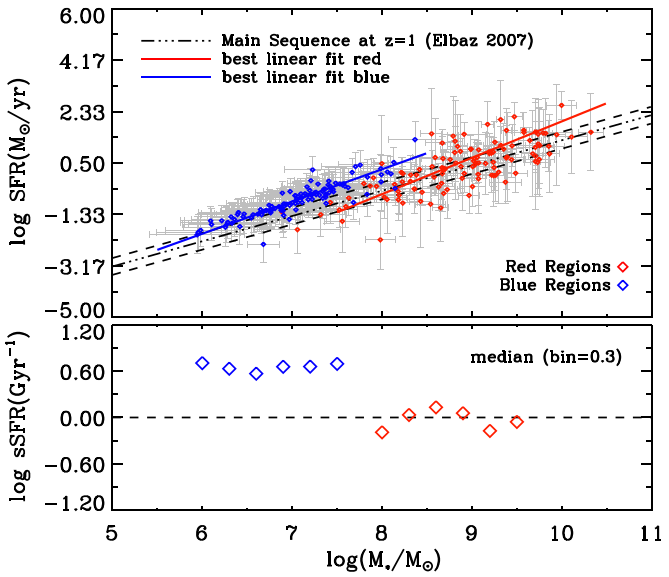

Figure 12. Top panel: median star formation rate with respect to median stellar mass for red (red diamonds) and blue (blue diamonds) regions in galaxies (1 red and 1 blue point for each galaxy in our sample). Linear fits to blue and red regions are plotted as solid lines. The dashed–dotted lines represent the extrapolation of the main sequence at $z \sim 1$ (Elbaz et al. 2007; best fit and 1σ). In the bottom panel, the median sSFR in blue and red regions is plotted in stellar mass bins of 0.3 dex.

(A color version of this figure is available in the online journal.)

7. DISCUSSION

In studies of the evolution of galaxies, samples are often divided into two broad populations: actively star-forming and passive. However, studying resolved maps of star-forming galaxies at kiloparsec scales,we found different modes of galaxy

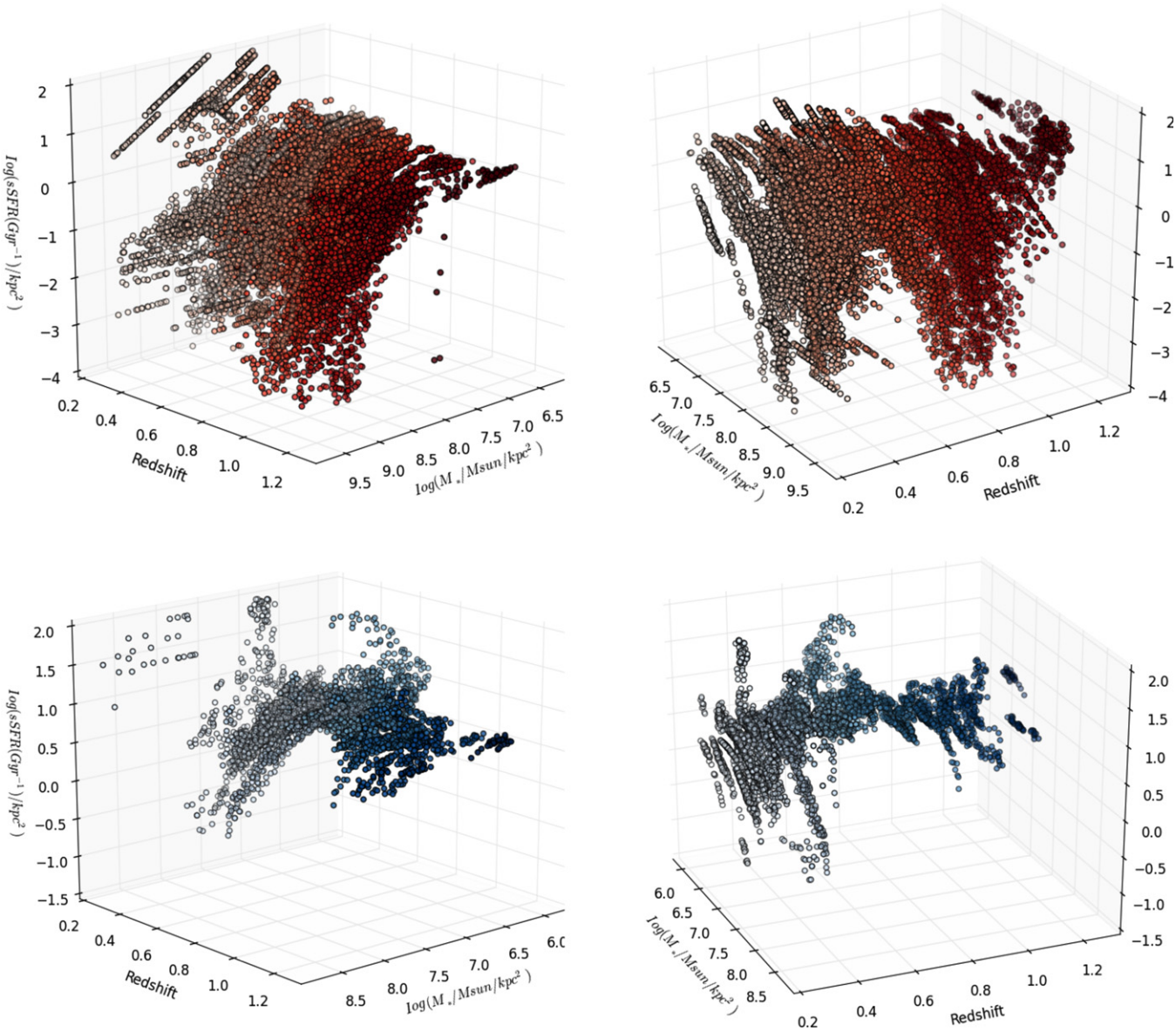

Figure 13. sSFR plotted as a function of stellar mass and redshift for resolution elements associated with red (top) and blue (bottom) regions at two different projections (right/left). Each point is color coded based on redshift.

(A color version of this figure is available in the online journal.)

growth within a given galaxy with sSFR differing over an order of magnitude (sometimes even more) from region to region.

Red regions on average have higher mass surface densities and are older compared to bluer regions in galaxies out to $z \sim 1.3$. Using our method, we find that the covering fraction of red regions is always greater than blue regions and that the covering fraction of these regions does not evolve significantly with redshift or the total stellar mass of the galaxy in the redshift ($0.2 < z < 1.3$) and stellar mass ($\mathrm{Log}(M_*/M_{\mathrm{sun}}) \sim 8.5$–$11.0$) range examined in this study. We also show that blue regions are farther away from the center of the galaxy (between 2 and 4 scale radii of the galaxy) compared to red regions (typically within 1 scale radius) with blue regions showing a larger dispersion. For both blue and red regions, the distance from the center as normalized by the scale radius is not evolving with redshift, however, more variation is seen with the stellar mass of the galaxy. In more massive systems, the distribution of red regions tends to be tightly confined to the center, with a much smaller dispersion compared to less massive galaxies, while the dispersion remains larger for blue regions. More generally, the clear distinction between the radial distribution of red and blue regions becomes much less distinct in the lowest mass galaxies as opposed to the high mass objects. In future works, we will investigate how properties of these red and blue regions relate to the morphology of the host galaxy, specifically substructures in galaxies with disturbed morphologies, including instabilities and merger remnants.

We find that red regions have already formed the bulk of their stars where relatively more star formation per stellar mass surface density persists in the blue regions. This appears to be driven by the difference in stellar mass surface density between red and blue regions rather than systematic differences in the SFR itself. The decline in sSFR with redshift is thus seen for all regions but the declining rate depends on the stellar mass with more massive regions declining with steeper slopes compared to less massive ones.

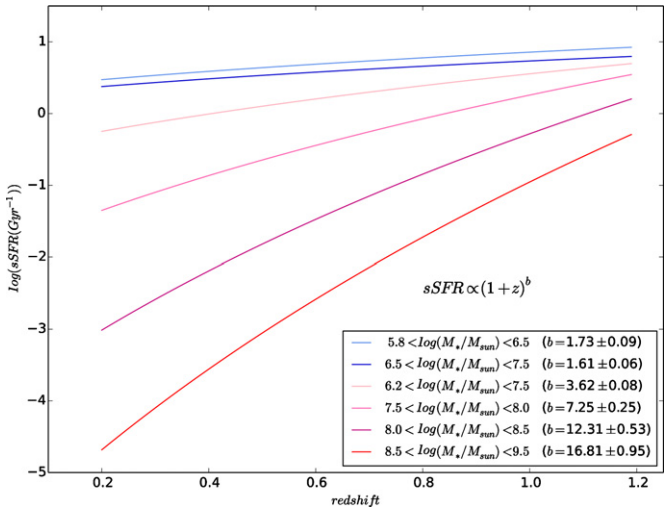

Figure 14. Redshift evolution of specific SFR: red and blue lines represent the best fit to the resolution elements in red and blue regions binned by stellar mass surface density, respectively.

(A color version of this figure is available in the online journal.)

The emerging picture is that centrally located red regions cover more galaxy surface area relative to the blue regions in the outer disk, as expected given that the highest stellar mass surface densities are found in galaxy centers (in bulges, pseudo-bulges, or simply the central peak of the disk profile) and regions of higher sSFRs are found farther out in the relatively bluer galaxy/disks. We are indeed seeing a difference in stellar mass surface density and dust combined with younger ages in blue regions rather than elevated levels of star formation per se as compared to red regions.

Put another way, if the SFRs have similar distributions between red and blue regions, why do we still detect blue $U - V$ color regions given the smoothness of stellar mass surface density maps? By process of elimination, it is the stellar ages, metallicities, and/or dust distributions that are left as the probable causes of blue regions observed in the outer disks. While we know degeneracies exist in fitting these properties via SEDs, it is unclear if these compounded degeneracies are enough to falsely manufacture a $\sim$1 Gyr spread between median ages in red and blue regions (Figure 11). Uneven distributions of metals in pockets left over from previous generations of stars could be at play on their way to being smoothed out by the mixing orbits of typical disk dynamics. Ultimately though, blue regions are either caused by a relatively higher fraction of bright, short-lived O and B stars being formed in the region and/or windows in the dust just above the disk (dust that is elsewhere denser and absorbing the light escaping from, e.g., the denser, dustier galaxy core). The UV light of a small population of young stars could possibly be completely obscured from our view in red regions which are regions of thicker stellar disks/bulges and thus more affected by absorption. However, if this is not the case, then why exactly are such different populations of stars forming in red regions versus blue regions given a universal IMF?

By overlooking the small-scale properties of galaxies when studying their global properties, the whole picture is not revealed. In future work, we plan to address these questions by further application of the tools developed in this paper to leverage deep spectral profiles across galaxies in this sample. We aim to learn more about the evolution of metallicity profiles, rotation curve decomposition, and comparative dynamical and star-formation timescales derived from both the photometric and spectroscopic properties of our data.

8. SUMMARY

In this paper, we have studied the resolved kiloparsec-scale structures in a unique sample of 119 disk galaxies in the GOODS fields using the highest resolution *HST* images from optical to near-infrared bands, taken as a part of the CANDELS project. This sample has extraordinarily deep spectroscopic observations with Keck DEIMOS, including precise measures of their rotation curves, allowing for not only a more detailed dynamical study using these maps but also other spectroscopically enabled studies using stellar absorption and emission lines (e.g., metallicity gradients across the galaxies, etc.). The main points of this first paper are summarized as follows.

1. We develop and test a method to generate spatially resolved rest-frame color, stellar mass, age, SFR, and extinction maps of galaxies with *HST* resolution, allowing for differences in PSFs from different instruments and testing against redshift-dependent biases.
2. We compared the stellar mass surface density, SFR surface density, and stellar ages measured by resolved SED fitting to the integrated stellar masses, SFRs, and ages. We found a good agreement with offsets of 0.04 dex, 0.16 dex, and 0.02 dex for stellar mass, SFR, and age, respectively.
3. We find that the stellar mass distribution in the disks are very smooth and 30%–90% of the total stellar mass comes from the central 2.5 kpc of the galaxies of our sample.
4. Developing a method to define statistically significant regions within galaxies, we identified "blue" and "red" regions in the two-dimensional color maps and investigated their physical properties. In the majority of galaxies in our sample, the rest-frame $(U - V)$ color maps covering the Balmer/4000 Å break have red centers with most blue regions located in the outer parts of the galaxies. We find a few exceptions with blue nuclei ($N = 3$ in this sample), which host AGNs, given the X-ray detection within 1 arcsec of their centers in each of these cases.
5. We show that there is a bimodality between red and blue regions on the SFR–mass plane, with the red regions having a higher stellar mass surface density compared to blue regions at each fixed SFR. The relation is much tighter for blue regions with a slope of 1.1 ± 0.1 compared to red regions with a slightly steeper slope of 1.3 ± 0.1.
6. Fitting the sSFR as a function of redshift for different stellar mass bins, we see more massive regions having smaller sSFRs at each redshift. We quantify the rate of sSFR decline with redshift for different mass bins in blue and red regions. We find that this decline is driven primarily by the stellar mass surface densities rather than the SFRs at a given resolution element.

We thank the anonymous referee for the extensive review and constructive comments on this manuscript. We thank Richard Ellis, Jeff Newman, and Behnam Darvish for helpful comments that improved the quality of this work. This work is based on observations taken by the CANDELS Multi-Cycle Treasury Program with the NASA/ESA *HST*, which is operated by the Association of Universities for Research in Astronomy, Inc., under NASA contract NAS5-26555. The authors thank NASA and STScI for *HST* Theory/Archival grant AR-13259. D.K.

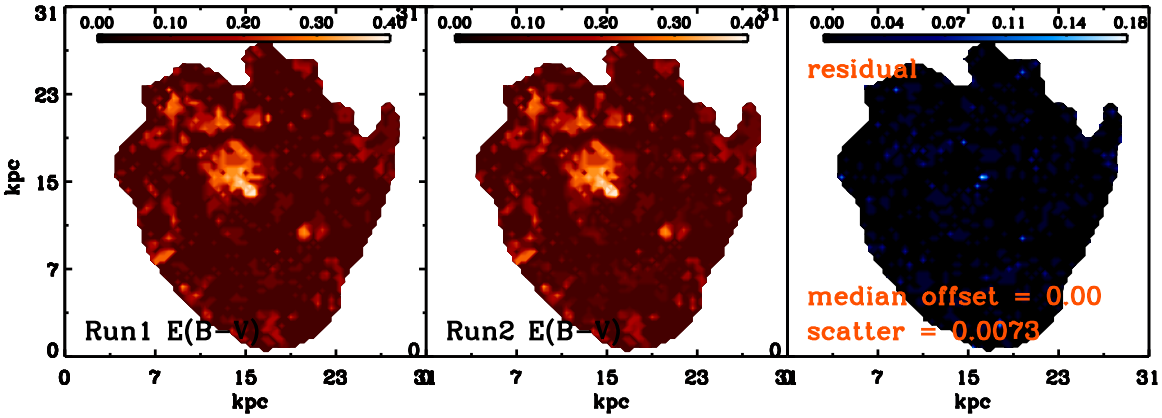

Figure 15. Comparison of $E(B-V)$ maps from Run1 and Run 2 for a galaxy in our sample. Run 2 has a higher resolution in extinction levels compared to Run1.
(A color version of this figure is available in the online journal.)

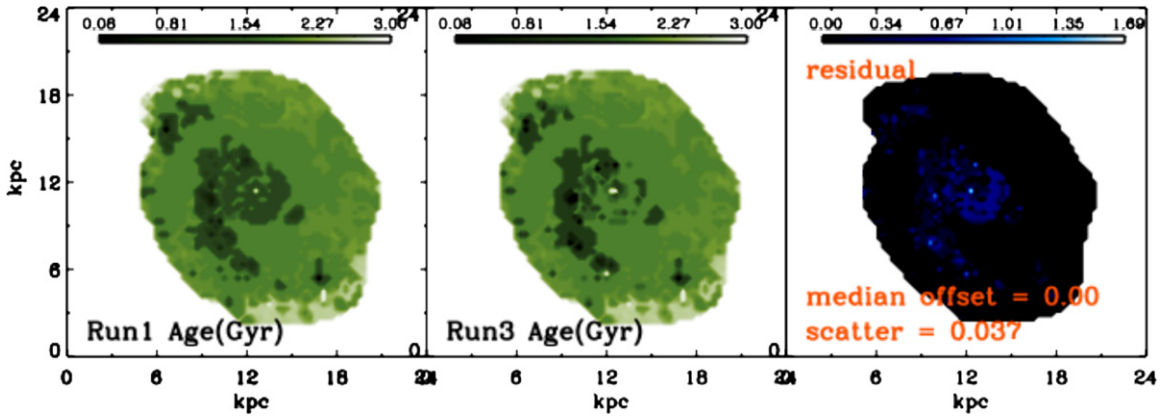

Figure 16. Comparison of age maps from Run 1 and Run 3 for a galaxy in our sample. Run 3 has less resolution in age levels compared to Run1.
(A color version of this figure is available in the online journal.)

acknowledges partial support from NSF grant AST-0808133. We thank R. Ellis, K. Bundy, T. Treu, and K. Chiu for their part in the initial assembly of the spectroscopic data set that this sample is based on, presented in Miller et al. (2011).

APPENDIX

CHOICE OF GRID FOR MODEL LIBRARIES

The physical parameters measured by fitting the SED of the integrated light of galaxies or individual pixels are drawn from a library of model SEDs. This means that choices in the discrete nature of model libraries affects the estimated output parameters. Many studies look at the effect of these choices, including their uncertainties, on the integrated (see, e.g., Conroy 2013; Ilbert et al. 2010) or resolved (see, e.g., Welikala et al. 2011) SED fitting results. In this Appendix, we analyze the effect of some of our assumptions regarding the model library on the output parameters.

To inspect how choosing a particular grid of input parameters for the library affects our SED fitting output estimates and therefore the maps, we select nine representative galaxies from our sample spanning the whole redshift range studied in this work ($0.2 < z < 1.2$). We fit the SED per resolution element following the methods described in Section 3 using different libraries. We change one parameter in the library at a time while keeping all the other library parameters the same (see Table 2).

Table 2
Model Library Parameters for Test Runs

Run	SFH	τ (Gyr)	$E(B-V)$	Age (Gyr)	Metallicity (Z_{solar})
1	Declining	21: 0.01–10.0	15: 0–1.0	57: 0.01–13.5	40%
2	Declining	21: 0.01–10.0	**21: 0–1.0**	57: 0.01–13.5	40%
3	Declining	21: 0.01–10.0	15: 0–1.0	**40: 0.01–13.5**	40%
4	Declining	21: 0.01–10.0	15: 0–1.0	57: 0.01–13.5	**100%**
5	Declining	21: 0.01–10.0	15: 0–1.0	57: 0.01–13.5	**20%**

Note. The bold values are the variables at each SED fitting test.

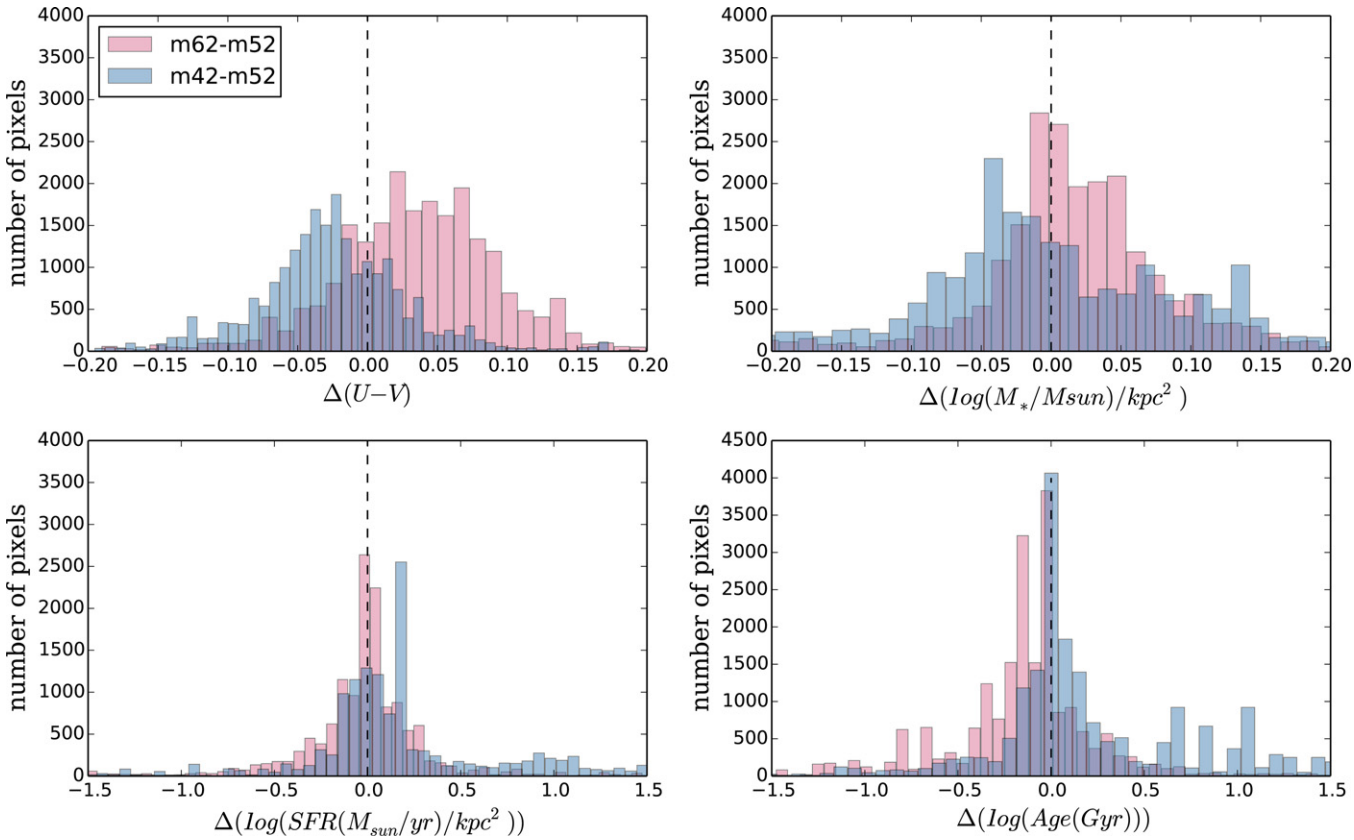

Figure 17. Effect of metallicity on rest-frame $(U-V)$, stellar mass surface density, SFR surface density, and stellar age. Red and blue colors correspond to $\Delta(m62-m52)$ (Run 4-Run 1) and $\Delta(m42-m52)$ (Run 5-Run 1), respectively.

(A color version of this figure is available in the online journal.)

Table 3
Stellar Metallicity Effection in SED Fitting

	$(U-V)$ (Rest-frame)	Log(ΣM_*) ($M_{\rm sun}$ kpc^{-2})	Log(ΣSFR) ($M_{\rm sun}$ yr^{-1} kpc^{-2})	Log(Age) (Gyr)
Run4–Run1 median offset	0.04	0.01	−0.01	−0.12
Run4–Run1 dispersion	0.06	0.09	0.53	1.14
Run5–Run1 median offset	−0.03	−0.01	0.14	0.11
Run5–Run1 dispersion	0.06	0.14	0.77	1.6

We then compare the measurements at resolution elements. The first run (Run1) is performed using the library described in Section 3 and all the other measurements will be compared to this one. The next two runs (Run2 and Run3) are generated by changing the resolution in extinction and age. Ideally, one would expect the highest resolution grids to produce smoother maps, but in reality, arbitrarily increasing the library size could lead to more degeneracies (e.g., Walcher et al. 2011), in the χ^2 fitting of the SEDs, let alone the high computational cost. Finally, in the last two runs (Run4 and Run5), we examine the outcome by changing stellar metallicity to solar (m62) and then to 20% solar (m42).

We compare the $E(B-V)$ maps from the first two runs in which we increase the number of steps in extinction by 25%. Subtracting the two maps, we see a median offset of 0.0 and a scatter in the range of 0.0–0.02. The small median difference and scatter should not be a surprise as we have only changed the resolution and not the range. In Figure 15, we plot the extinction maps for one of the galaxies using the two libraries and their difference. This figure demonstrates the point that extinction maps produced from the two runs are visually indistinguishable. The same has been seen for all the test galaxies. Even though there are small differences at some individual resolution elements, the overall structure and patterns remain intact.

The same situation holds, comparing the age maps from the third run to those from the first, with the overall trends not changing but slightly larger offset resolution element by resolution element (Figure 16). The median offset is 0.0 for all the test galaxies, but there is a larger scatter in the range of 0.01–0.1. The difference in each resolution element is always well below its 1σ uncertainty of that resolution element in both runs. This does not necessarily mean that the difference is small for all resolution elements, but rather it shows that for resolution elements with less constrained probability distribution functions (PDFs) the resolution can play an important role.

In the last two runs we study the dependence of the parameters on variations in metallicity. We change the metallicity once to solar (m62) and once to 20% solar (m42) and compare the physical parameters with the first run which has metallicity fixed to 40% solar (m52). This is shown in Figure 17, where red and blue histograms correspond to $\Delta(m62-m52)$ (Run4-Run1) and

$\Delta(m42 - m52)$ (Run5-Run1), respectively. The median offset and dispersion in rest-frame $(U - V)$ color, stellar mass, SFR, and stellar age over all resolution elements in the test galaxies are listed in Table 3.

In this work, we fixed the metallicity to 40% solar and produced maps of physical properties of galaxies. We selected regions based on $(U - V)$ rest-frame color. Having fixed the metallicity to a higher or lower value, the same regions would have been identified but with slightly offseted properties, as quantified in the above table. This is because the region selection is based on the color distribution in each galaxy and does not assume a predefined cut. This is of course different from having the metallicity as a free parameter, which will expand the degeneracies, especially with age. We find that assuming stellar metallicity leads to redder $(U - V)$ rest-frame colors, slightly larger masses, no significant change in median SFR (although significant scatter), and younger ages. Finally, further work is needed to fully uncover the effects of all different grid parameter choices (from IMF and SSPs to star formation histories) on resolved SED fitting results.

REFERENCES

Abraham, R. G., Ellis, R. S., Fabian, A. C., Tanvir, N. R., & Glazebrook, K. 1999, MNRAS, 303, 641
Arnouts, S., Cristiani, S., Moscardini, L., et al. 1999, MNRAS, 310, 540
Barden, M., Jahnke, K., & Häußler, B. 2008, ApJS, 175, 105
Bell, E. F., Papovich, C., Wolf, C., et al. 2005, ApJ, 625, 23
Bell, E. F., Phleps, S., Somerville, R. S., et al. 2006, ApJ, 652, 270
Bell, E. F., van der Wel, A., Papovich, C., et al. 2012, ApJ, 753, 167
Bell, E. F., Wolf, C., Meisenheimer, K., et al. 2004, ApJ, 608, 752
Bertin, E., & Arnouts, S. 1996, A&AS, 117, 393
Bruzual, G., & Charlot, S. 2003, MNRAS, 344, 1000
Chabrier, G. 2003, PASP, 115, 763
Conroy, C. 2013, ARA&A, 51, 393
Cowie, L. L., Songaila, A., Hu, E. M., & Cohen, J. G. 1996, AJ, 112, 839
Daddi, E., Bournaud, F., Walter, F., et al. 2010, ApJ, 713, 686
Daddi, E., Dickinson, M., Morrison, G., et al. 2007, ApJ, 670, 156
Damen, M., Förster Schreiber, N. M., Franx, M., et al. 2009, ApJ, 705, 617
Dekel, A., Sari, R., & Ceverino, D. 2009, ApJ, 703, 785
Dickinson, M., Papovich, C., Ferguson, H. C., & Budavári, T. 2003, ApJ, 587, 25
Elbaz, D., Daddi, E., Le Borgne, D., et al. 2007, A&A, 468, 33
Elmegreen, B. G., Bournaud, F., & Elmegreen, D. M. 2008, ApJ, 688, 67
Faber, S. M., Phillips, A. C., Kibrick, R. I., et al. 2003, Proc. SPIE, 4841, 1657
Faber, S. M., Willmer, C. N. A., Wolf, C., et al. 2007, ApJ, 665, 265
Feulner, G., Goranova, Y., Drory, N., Hopp, U., & Bender, R. 2005, MNRAS, 358, L1
Förster Schreiber, N. M., Genzel, R., Bouché, N., et al. 2009, ApJ, 706, 1364
Genzel, R., Newman, S., Jones, T., et al. 2011, ApJ, 733, 101
Giavalisco, M., Ferguson, H. C., Koekemoer, A. M., et al. 2004, ApJL, 600, L93
Grogin, N. A., Kocevski, D. D., Faber, S. M., et al. 2011, ApJS, 197, 35
Guo, Y., Giavalisco, M., Ferguson, H. C., Cassata, P., & Koekemoer, A. M. 2012, ApJ, 757, 120
Hopkins, P. F., Bundy, K., Croton, D., et al. 2010, ApJ, 715, 202
Ilbert, O., Arnouts, S., McCracken, H. J., et al. 2006, A&A, 457, 841
Ilbert, O., Salvato, M., Le Floc'h, E., et al. 2010, ApJ, 709, 644
Kassin, S. A., Weiner, B. J., Faber, S. M., et al. 2012, ApJ, 758, 106
Kauffmann, G., Heckman, T. M., White, S. D. M., et al. 2003, MNRAS, 341, 33
Koekemoer, A. M., Faber, S. M., Ferguson, H. C., et al. 2011, ApJS, 197, 36
Kriek, M., Labbé, I., Conroy, C., et al. 2010, ApJL, 722, L64
Kriek, M., van Dokkum, P. G., Whitaker, K. E., et al. 2011, ApJ, 743, 168
Lang, P., Wuyts, S., Somerville, R., et al. 2014, ApJ, 788, 11
Lanyon-Foster, M. M., Conselice, C. J., & Merrifield, M. R. 2007, MNRAS, 380, 571
Lanyon-Foster, M. M., Conselice, C. J., & Merrifield, M. R. 2012, MNRAS, 424, 1852
Lilly, S. J., Carollo, C. M., Pipino, A., Renzini, A., & Peng, Y. 2013, ApJ, 772, 119
Lilly, S. J., Le Fevre, O., Hammer, F., & Crampton, D. 1996, ApJL, 460, L1
Lin, L., Koo, D. C., Willmer, C. N. A., et al. 2004, ApJL, 617, L9
Lotz, J. M., Jonsson, P., Cox, T. J., et al. 2011, ApJ, 742, 103
Madau, P., Pozzetti, L., & Dickinson, M. 1998, ApJ, 498, 106
Maraston, C., Daddi, E., Renzini, A., et al. 2006, ApJ, 652, 85
Maraston, C., Pforr, J., Renzini, A., et al. 2010, MNRAS, 407, 830
Miller, S. H., Bundy, K., Sullivan, M., Ellis, R. S., & Treu, T. 2011, ApJ, 741, 115
Mobasher, B., Dahlen, T., Hopkins, A., et al. 2009, ApJ, 690, 1074
Nayyeri, H., Mobasher, B., Hemmati, S., et al. 2014, ApJ, 794, 68
Noeske, K. G., Weiner, B. J., Faber, S. M., et al. 2007, ApJL, 660, L43
Oke, J. B., & Gunn, J. E. 1983, ApJ, 266, 713
Papovich, C., Dickinson, M., & Ferguson, H. C. 2001, ApJ, 559, 620
Patton, D. R., Pritchet, C. J., Carlberg, R. G., et al. 2002, ApJ, 565, 208
Pickles, A. J. 1998, PASP, 110, 863
Reddy, N. A., Pettini, M., Steidel, C. C., et al. 2012, ApJ, 754, 25
Reddy, N. A., Steidel, C. C., Fadda, D., et al. 2006, ApJ, 644, 792
Rudnick, G., Rix, H.-W., Franx, M., et al. 2003, ApJ, 599, 847
Salim, S., Dickinson, M., Michael Rich, R., et al. 2009, ApJ, 700, 161
Salmon, B., Papovich, C., Finkelstein, S. L., et al. 2014, e-print (arXiv:1407.6012)
Schade, D., Lilly, S. J., Crampton, D., et al. 1995, ApJL, 451, L1
Scott, D. W. 1979, Biometrika, 66, 605
Shapley, A. E., Steidel, C. C., Adelberger, K. L., et al. 2001, ApJ, 562, 95
Tacconi, L. J., Neri, R., Genzel, R., et al. 2013, ApJ, 768, 74
van de Voort, F., Schaye, J., Booth, C. M., & Dalla Vecchia, C. 2011, MNRAS, 415, 2782
Walcher, J., Groves, B., Budavári, T., & Dale, D. 2011, Ap&SS, 331, 1
Welikala, N., Hopkins, A. M., Robertson, B. E., et al. 2011, e-print (arXiv:1112.2657)
Whitaker, K. E., Franx, M., Leja, J., et al. 2014, ApJ, 795, 104
Wuyts, S., Förster Schreiber, N. M., Genzel, R., et al. 2012, ApJ, 753, 114
Wuyts, S., Förster Schreiber, N. M., Nelson, E. J., et al. 2013, ApJ, 779, 135
Wuyts, S., Förster Schreiber, N. M., van der Wel, A., et al. 2011, ApJ, 742, 96
Zibetti, S., Charlot, S., & Rix, H.-W. 2009, MNRAS, 400, 1181